Title

Cell position-based evaluation of mechanical features of cells in multicellular systems

Short title

Mechanical features from cell position

Authors

Hiroshi Koyama[1,2,*], Atsushi M. Ito[2,3], Hisashi Okumura[2,4,5], Tetsuhisa Otani[2,6,7], Kazuyuki Nakamura[8,9], and Toshihiko Fujimori[1,2]

[1]Division of Embryology, National Institute for Basic Biology, 5-1 Higashiyama, Myodaiji, Okazaki, Aichi 444-8787, Japan

[2]SOKENDAI (The Graduate University for Advanced Studies), Hayama, Kanagawa 240-0193, Japan

[3]National Institute for Fusion Science, National Institutes of Natural Sciences, 322-6 Oroshi-cho, Toki, Gifu 509-5292, Japan

[4]Biomolecular Dynamics Simulation Group, Exploratory Research Center on Life and Living Systems (ExCELLS), National Institutes of Natural Sciences, 5-1 Higashiyama,

Myodaiji, Okazaki, Aichi 444-8787, Japan

[5]Institute for Molecular Science, National Institutes of Natural Sciences, 5-1 Higashiyama, Myodaiji, Okazaki, Aichi 444-8787, Japan

[6]Division of Cell Structure, National Institute for Physiological Sciences, 5-1 Higashiyama, Myodaiji, Okazaki, Aichi 444-8787, Japan

[7]Laboratory of Cell Biology and Biochemistry, Department of Biological Sciences, Tokyo Metropolitan University, 1-1 Minami-Osawa, Hachioji 192-0397, Tokyo, Japan.

[8]School of Interdisciplinary Mathematical Sciences, Meiji University, 4-21-1 Nakano, Nakano-ku, Tokyo 164-8525, Japan

[9]JST, PRESTO, 4-1-8 Honcho, Kawaguchi, Saitama 332-0012, Japan

Myodaiji, Okazaki, Aichi 444-8585, Japan

*Correspondence: Hiroshi Koyama

Division of Embryology, National Institute for Basic Biology, 5-1 Higashiyama, Myodaiji, Okazaki, Aichi 444-8787, Japan

Phone: +81 564 59 5862,

hkoyama@nibb.ac.jp.

Conflicts of interest

The authors declare no competing financial interests.

Keywords

effective potential, cell–cell interaction, image-based force inference, mechanics, particle model, vertex model

This file includes:

- Main text
- Figure 1 to 8
- Table 1

Abstract

Measurement of mechanical forces of cell–cell interactions is important for studying the emergence of diverse three-dimensional morphologies of multicellular organisms. We previously reported an image-based statistical method for inferring effective pairwise forces of cell–cell interactions (i.e., attractive/repulsive forces), where a cell particle model was fitted to cell tracking data acquired by live imaging. However, because the particle model is a coarse-grained model, it remains unclear how the pairwise forces relates to sub-cellular mechanical components including cell–cell adhesive forces. Here we applied our inference method to cell tracking data generated by vertex models that assumed sub-cellular components. Through this approach, we investigated the relationship between the effective pairwise forces and various sub-cellular components: cell–cell adhesion forces, cell surface tensions, cell–extracellular matrix (ECM) adhesion, traction forces between cells and ECM, cell growth, etc. Some sub-cellular components showed attractive or repulsive effect. This comprehensive analysis provides theoretical bases for linking the pairwise forces to sub-cellular mechanical components.

Introduction

In multicellular living systems, mechanical features of cells are critical parameters for morphogenesis. For instance, epithelial cells show tightly packed cell configuration with polygonal shapes, where both cell–cell adhesive forces and cell surface tensions are major components for regulating cell shapes, fluidity of the tissues, and tissue deformation (Bi et al., 2015; Landsberg et al., 2009; Lecuit et al., 2011). To address the roles of the mechanical components of cell in the behaviors of whole systems, several frameworks for simulating multicellular systems have been developed such as vertex models, cell particle models, Cellular Potts models, phase field models, etc (Merkel and Manning, 2017; Nonomura, 2012).

To perform simulations, mechanical parameters are required that are measured by using techniques such as atomic force microscopies (Campàs, 2016; Sugimura et al., 2016) or by using image-based force inference methods (Brodland et al., 2010; Ishihara and Sugimura, 2012; Koyama et al., 2023). The latter enable us to acquire spatio-temporal information of parameter values. For instance, by fitting a vertex model to microscopic images with labeled cell membranes, cell–cell junction tensions were inferred (Ishihara and Sugimura, 2012). In the case of three-dimensional (3D) tissues, due to the difficulties of imaging cell membranes with subsequent segmentation, we previously reported a

88 particle model-based force inference method where only cell nuclear positions were used
89 as described later in detail (Koyama et al., 2023). In other words, this inference method
90 is based on nuclear/cellular positions with temporal evolution. However, because a
91 particle model is a coarse-grained model, it is not clear how the forces in the particle
92 model relate to sub-cellular mechanical parameters including cell–cell adhesion forces.

93 The cell particle models, where a cell is described as a point particle as a coarse-
94 grained description, have been widely applied to various cells including blastomeres,
95 cancer cells, mesenchymal cells, and epithelial cells (Drasdo et al., 1995; Forgacs and
96 Newman, 2005; Guillot and Lecuit, 2013; Maître et al., 2012; Merkel and Manning, 2017;
97 Steinberg, 2007; Yong et al., 2015). The particle models typically assume both attractive
98 and repulsive forces of cell–cell interactions: i.e., mechanical potential of pairwise cell–
99 cell interactions. Because of their simplicity, low coding cost, and low computational load,
100 the particle models are advantageous for simulating larger three-dimensional systems
101 (Delile et al., 2017; Nissen et al., 2018). However, the origin(s) of the attractive/repulsive
102 forces has not been correctly clarified. For instance, questions to be addressed include
103 whether attractive behaviors of cell–cell interactions are conferred from cell–cell
104 adhesion forces, etc. This issue is important to correctly interpret outcomes obtained by
105 simulations based on the particle models with the relation to the sub-cellular mechanical

features.

In the case of isolated two cell systems (Fig. 1A-B), cell–cell adhesion forces should shorten the cell–cell distance, which can be described as an effective attractive force, whereas both cell surface tensions and excluded volume effect of the cells can be described as an effective repulsive force, as described in text books and in some articles (Forgacs and Newman, 2005; Merkel and Manning, 2017). Then, the summation of these different forces may lead to distance-dependent force curves (Fig. 1C). However, it remains unclear whether the above relationships considered in the isolated two cell systems are applicable to multicellular systems (Fig. 1D), because cells in multicellular systems can exhibit shapes far from spheres and so on.

In the present study, we aimed to extend the cell position-based force inference framework. By using our image-based method for inferring effective distance–force curves (Koyama et al., 2023), we theoretically evaluated the relationships between the effective distance–force curves and the sub-cellular mechanical components. In other words, by applying our inference method to synthetic data generated by simulating vertex models where cell–cell adhesion forces and cell surface tensions are explicitly assumed, we evaluated the relationship between the distance–force curves and the sub-cellular mechanical components (Fig. 1D). In addition to these components, we also consider

following sub-cellular components: the area elasticity (conservation of cell volume/area), cell growth (cell volume increase), adhesion forces between cells and extracellular matrix (ECM), and traction forces between cells and ECM. This comprehensive analysis provides the information whether each sub-cellular component effectively works as attractive or repulsive, and also provide relationships between the particle models and other models including the vertex model.

Theory

Method for inferring attractive/repulsive forces of cell–cell interactions

To infer the effective attractive and repulsive forces of cell–cell interactions in multicellular systems, we previously developed an image-based inference method (Koyama et al., 2023). Several studies have been adopting image-based strategies for inferring cellular mechanical forces and properties (Brodland et al., 2010; Ishihara and Sugimura, 2012). In the case of our method, a particle model was fitted to temporal evolution of cell positions obtained from microscopic live imaging, which enabled us to infer attractive/repulsive forces between each cell–cell interaction with each time frame as explained below. By analyzing the inferred attractive/repulsive forces, we reported that

142 the effective attractive/repulsive forces can be actually approximated as a function
143 dependent on cell–cell interactions (i.e., distance–force curves similar to Fig. 1C) in
144 blastomeres of the mouse and of *C. elegans* embryos (Koyama et al., 2024, 2023).

145 Briefly, in our method, we minimized a following cost function; $G = G_{xyz} + G_{F_0}$,
146 where G_{xyz} is the difference between *xyz*-coordinates of each particle of *in vivo* data and
147 particle simulations, and G_{F_0} is the additional cost function for cell–cell distance-
148 dependent weight as previously defined (Koyama et al., 2023) (Supplementary
149 information). Our inference method was previously validated by applying this method to
150 simulation data generated under pregiven forces (Koyama et al., 2023).

151

152 Particle model to be fitted

153 The particle model to be fitted is as follows. Attractive and repulsive forces for pairwise
154 cell–cell interactions are assumed. Due to the low Reynolds number in the case of
155 cellular-level phenomena, the inertial force is negligible (Fletcher et al., 2014; Forgacs
156 and Newman, 2005; He et al., 2014; Li et al., 2017; Schötz et al., 2008). In the present
157 study, we assumed that cells are put on substrates, and that frictional forces between the
158 cells and the substrates are exerted, and the motion of the particles is overdamped by the
159 friction. In the case that the substrates are fixed (i.e, non-moving), the equation of a

particle motion may be written as $V_{\mathrm{C}|p} = F_{\mathrm{C}|p} / \gamma_{\mathrm{C}}$ for each particle, where $V_{\mathrm{C}|p}$ is the velocity of the *p*th particle, $F_{\mathrm{C}|p}$ is the summation of cell–cell interaction forces exerted on the *p*th particle, and γ_{C} is the coefficient of viscous drag and frictional forces provided from the substrates. This assumption has been used in both particle-based models and vertex models (Honda et al., 2008; Li et al., 2017; Nissen et al., 2017; Suzuki et al., 2017; Szabó et al., 2006).

During this inference, we assumed the simplest situation, where γ_{C} is constant (=1.0) as the same setting in our previous work (Koyama et al., 2023). The dimension of particle velocity $V_{\mathrm{C}|p}$ was set to be μm/min for convenience, which is typical dimension in analyses of living cells. Because we did not measure the value of γ_{C} in living tissues, we cannot determine the value of the effective force $F_{\mathrm{C}|p} (= \gamma_{\mathrm{C}} V_{\mathrm{C}|p})$ with a specific dimension. However, under the above assumption, 1 arbitrary unit (A.U.) of *F* coincides to a force which can move a particle with a velocity of 1 μm/min in tissues.

Vertex model simulation as synthetic data

As well-defined systems, we adopted the vertex model for describing epithelial cells which typically exhibit polygonal shapes (Fig, 2A, “Model”). This model is the standard framework for simulating epithelial cells, where some sub-cellular mechanical

components such as cell–cell adhesion forces and cell surface tensions are assumed (Fletcher et al., 2014; Okuda et al., 2015). By using the vertex model, we performed simulations, and we considered the simulation outcomes as synthetic data (Fig. 2A, "Simulation"). In other words, we applied our inference method to cell tracking data generated by the simulations of the vertex model, and then obtained effective distance–force curves (Fig. 2A, "DF curve").

The vertex model used in this study is essentially the same as that in our previous studies (Koyama et al., 2022; Suzuki et al., 2017). The potential energy in the whole system is defined as: $U = \sum_{<k,l>} \lambda_{\mathrm{Tot}} L^{<k,l>} + \sum_{n} \frac{1}{2} K_{\mathrm{a}} \left(\frac{a_n}{a_{\mathrm{O}}} - 1 \right)^2 a_{\mathrm{O}}$. λ_{Tot} is the line tension exerted on cell–cell junctions or on cell edges of outer boundary (Fig. 2A, "Model"). The line tension is provided from both the cell–cell adhesion force (λ_{AD}) and the cell surface tension (λ_{S}); the former has a negative effect on the line tension, and the latter does a positive (Fig. 2A; $\lambda_{\mathrm{Tot}} = 2\lambda_{\mathrm{S}} - \lambda_{\mathrm{AD}}$). The potential energy on a junction or edge is $\lambda_{\mathrm{Tot}} L^{<k,l>}$, where L is the length of the junction or edge composed of kth and lth vertices. The potential energy for a cell provided by the area elasticity is $(1/2)K_{\mathrm{a}} \left(a_n / a_{\mathrm{o}} - 1 \right)^2 a_{\mathrm{o}}$, where a_n is the area of nth cell and a_{o} is the natural area. The force ($F_{\mathrm{V}|h}$) exerted on an hth vertex is calculated as follows: $F_{\mathrm{V}|h} = -\nabla U$, where ∇ is the nabla vector differential operator at each vertex. Similar to the particle model, we assumed that cells

are put on non-moving substrates with frictional forces. Therefore, the motion of each vertex is described as follows: $V_{\mathrm{V}|h} = F_{\mathrm{V}|h} / \gamma_{\mathrm{V}}$, $V_{\mathrm{V}|h}$ is the velocity of the *h*th vertex, and γ_{V} is the coefficient of the friction of a vertex. Similar to the case in the particle model, γ_{V} was set to 1.0, and the dimension of particle velocity $V_{\mathrm{V}|h}$ was set to be μm/min.

The fluctuation of the line tensions (σ) was assumed as follows. Cellular edges to be activated were selected according to p_{ED} which is the probability of activation per unit of time. On the cellular edges selected, σ was added to the line tensions, and the duration time of this activated state is τ as defined in the Supplementary information.

Results

Inference of attractive/repulsive forces in vertex model

To evaluate possible relationships between attractive/repulsive forces and cell–cell adhesion forces/cell surface tensions, we applied our inference method to synthetic cell tracking data generated by our vertex model. We performed simulations with several tens of cells (Fig. 2A, “Simulation”) and obtained cell tracking data.

Fig. 2B-i shows the plots of inferred forces against cell–cell distances. In the

214 absence of the fluctuations of tensions (0%), the distribution of the data points was not so
215 diverged (Fig. 2B-i, heat maps), and a DF curve was detected (Fig. 2B-i, binned average
216 (yellow). The binned averaged line in Fig. 2B-i is shown in Fig. 2B-ii (red line), which
217 exhibited a typical profile with a peak of the attractive force. In the presence of the
218 fluctuations, the distributions became wider (Fig. 2B-i, heat maps), but the DF curves
219 were detected whose profiles were equivalent to that without the fluctuations (Fig. 2B-ii).
220 In conclusion, effective DF curves are detectable in multicellular epithelial cells.
221
222 *Influence of cell–cell adhesion forces/cell surface tensions to DF curves*
223 Next, we examined whether microscopic features of epithelial cells were reflected into
224 the effective DF curves. We performed simulations under various values of the cell–cell
225 adhesion forces (Fig. 3A-i); the cells showed highly deformed cell shapes or regular
226 hexagonal shapes under the stronger or weaker cell–cell adhesion forces, respectively.
227 The inferred DF curves are shown in Fig. 3A-ii, whose profiles are quantitatively
228 evaluated in Fig. 3A-iii. The absolute values of the maximum attractive forces were
229 positively correlated with the cell–cell adhesion forces (Fig. 3A-iii). These results are
230 consistent with the case in the isolated two cell systems.
231 We also evaluated the effect of the cell surface tensions (Fig. 3B), and

successfully detected DF curves (Fig. 3B-i). The effect on the maximum attractive forces was opposite to the cell–cell adhesion forces (Fig. 3B-ii). Together with the results in the case of the cell–cell adhesion force, these results indicate that the effects of the microscopic features of the cells are conserved among multicellular epithelial cells and isolated two cell systems.

Finally, we evaluated the effect of the area elasticity. Under large area elasticity, one expectation is that the slope of the repulsive region in the DF curve becomes steeper due to its elasticity. The inferred effective DF curves and their quantitative evaluations are shown in Fig. 3C-i and 3C-ii. The typical profiles of DF curves such as the peak of the attractive forces were clearly detected, but the maximum values were not significantly affected by the area elasticity (Fig. 3C-ii). The profiles of the repulsive regions were not obtained in all conditions, though the slope under the higher value of the area elasticity (= 10.0) was steepest (Fig. 3C-i, purple line).

In summary, the cell position-based method for evaluating mechanical properties of multicellular epithelial cells revealed that the cell–cell adhesion forces and the cell surface tensions show attractive and repulsive effect, respectively.

Influence of cell-ECM adhesion to DF curve

In real tissues, there are various types of non-cellular external factors which affect cell behaviors; extracellular matrix (ECM), egg shells, liquid cavity, etc (Honda et al., 2008; Kajita et al., 2003). These factors may influence inferred effective DF curves. This is analogous to atomic, molecular, and colloidal sciences. For instance, external pressures increase the density of particulate objects, which is reflected into the radial distribution function linked to effective distance–potential curves (Atkins et al., 2018). Another example is solvents, where hydration of particles by the solvents yields energy barriers in effective distance–potential curves (Israelachvili, 2011). Therefore, by measuring effective distance–potential curves, one can predict, at least partially, what kind of external factors exist in systems of interest. In multicellular systems, however, it has not been clarified how external factors influence the effective distance–potential curves.

Here we examined the influence of ECM that interacts with cells. Spreading of cells is regulated by competition between cell–ECM and cell–cell adhesions; increased forces of cell–ECM adhesions lead to the increase in cell areas of epithelial cells (Fig. 4-i) (Pérez-González et al., 2019; Ryan et al., 2001; Yong et al., 2015). Because the increase in each cell area pushes surrounding cells away, we expected that the cell–ECM adhesion forces would function to repulsive effect on cell–cell interactions (Fig. 4-i, “Repulsive force?”). Simultaneously, increased cell areas lead to increases in distances between cells,

which should be reflected as a shift of effective DF curves to rightward along the cell–cell distances (Fig. 4-i, “Shift of DF curve?”).

We modeled cell–ECM adhesion in the vertex model used in Fig. 2. The potential energy was defined as $E_{\mathrm{ECM}} a_n$ for each cell, where E_{ECM} is the coefficient of the energy and a_n is the cell area as previously defined. Under increased cell–ECM adhesion forces, cell areas were increased (Fig. 4-ii, $E_{\mathrm{ECM}} = 1.0$ vs. $= 0.0$). Fig. 4-iii shows inferred effective DF curves, and Fig. 4-iv is the quantitative evaluation of the curves. As expected, the maximum attractive forces were negatively correlated with the cell–ECM adhesive forces (Fig. 4-iv, left panel), and the distances at the maximum attractive forces were increased by the cell–ECM adhesive forces (Fig. 4-iv, right panel). These results suggest that the cell–ECM adhesive forces are reflected into the effective DF curves as the reduced attractive forces.

Influence of cell-ECM traction forces to DF curve

Next, we focused on traction forces between cells and ECM, which confer self-migratory activities of the cells (Aoki et al., 2017; Garcia et al., 2015; Szabó et al., 2006). We implemented traction forces in the particle model instead of the vertex model, because there is no general way to implement self-migratory activities in vertex models. The

286 directions of the traction forces were set to be random (Fig. 5A-i, right panel), and persist
287 during a given time period (Fig. 5A-ii, "with persistency = 50.0min"). Cell–cell
288 interaction forces were provided by the Lennard-Jones (LJ) potential (Fig. 5A-i, "LJ").
289 The value of the traction forces is shown as a relative value to the maximum attractive
290 force of the LJ potential (Fig. 5A-ii, "1,000% of LJ"). Simulations were performed two-
291 dimensionally with the friction between the cells and the ECM.

292 Fig. 5A-iii shows inferred effective DF curves. In the absence of the traction
293 forces (0%), the inferred curve showed a similar profile to the given LJ potential (Fig.
294 5A-iii, purple line), though an inconsistency was observed at the distant region (distance
295 = ~7μm). In the case that the value of traction forces was equivalent to the attractive force
296 of the LJ potential (100%; light blue line), the curve was consistent with that without the
297 traction forces, whereas, under a larger traction force (1,000%; red line), the curve became
298 highly repulsive.

299 Fig. 5-iv shows the effects of persistency of the traction forces. Even under the
300 large traction forces (1,000%), a DF curve was consistent with that from the LJ potential
301 if the persistency was short (1.0min; purple line). In conclusion, traction forces can
302 significantly modify effective DF curves, if both the force value and the persistency are
303 large. Otherwise, the traction forces do not affect the profiles of DF curves. Similar

304 repulsive profiles of DF curves were obtained in the MDCK cells on substrates, which
305 have highly self-migratory activities (Fig. S1A).
306
307 *Influence of cell growth to DF curve*
308 Cell growth (i.e., cell volume increase during the cell proliferative phase) is an important
309 parameter for cell behaviors and homeostasis in multicellular systems: cell growth
310 increases pressure in multicellular systems, leading to contact inhibition of growth,
311 delamination in epithelial sheets, and apoptosis (Marinari et al., 2012; Podewitz et al.,
312 2015; Zimmermann et al., 2016). Under increased pressure, cells push/repel each other.
313 In other words, the intrinsic attractive forces between the cells may be effectively
314 cancelled due to cell growth. To test this hypothesis, we used a mathematical model
315 considering cell growth. A well-known cell growth model is shown in Fig. 6-i, where one
316 cell is modeled as two particles and the growth is described by the repulsive force
317 (coefficient B) between the two particles (Basan et al., 2011; Podewitz et al., 2015; Ranft
318 et al., 2010). The repulsive force is defined as follows; $B/(D+C)^2$, where D is the
319 distance between the paired two particles, and C is const (=5.6). When the distance
320 between the two particles reaches a critical value (D_{CR}=5.0), cell division occurs. In our
321 model, particle–particle interactions between different cells were implemented by the LJ

322 potential that was previously shown in Fig. 5A-iii, “LJ”. This model was originally
323 developed in three-dimensional cell aggregates with viscous frictions between the cells.
324 However, we modified this model so that the cell–substrate friction was assumed in a
325 similar manner to Fig 2-5 instead of the frictions between the cells.

326 We performed simulations and inferred effective DF curves between cells (Fig.
327 6-i, “DF curve” between the orange cells). When the cell growth coefficient B was set to
328 be larger, the cell number was increased (Fig. 6-ii, B = 4.0 vs. 0.0). Fig. 6-iii shows the
329 inferred effective DF curves, and Fig. 6-iv is their quantitative comparison. The maximum
330 attractive forces were negatively correlated with the growth forces, and eventually, the
331 attractive components were absolutely diminished (Fig. 6-iv). These results indicate that
332 cell growth effectively decreases attractive forces of cell–cell interactions.

333

334 *DF curve in vertex model under steady state*

335 In the above cases (Fig. 2-6), we assumed non-steady states: the systems are undergoing
336 morphological changes. Such non-steady states should be typical during morphogenesis
337 of multicellular systems. On the other hand, confluent epithelial monolayers show nearly
338 steady states, that may reflect tissues in adult organs. Under steady states, cells can
339 fluctuate, but do not experience morphological transitions; i.e., analogous to systems

340 under thermodynamically equilibrium states. By using the vertex model, we then
341 investigated the relationship between the effective DF curves and cell–cell adhesion
342 forces/cell surface tensions under steady states.

343 Fig. 7A shows a confluent epithelial monolayer modeled by the vertex model
344 where the vertices continuously moved due to the fluctuations of the line tensions of the
345 cell–cell junctions defined in Fig. 2. A whole view of the simulation is shown in Fig. S2.

346

347 *Influence of cell–cell adhesion forces/cell surface tensions to DF curve*

348 Fig. 7B shows the inferred effective DF curves under the conditions with different values
349 of cell–cell adhesion forces. In the all cases, distance–force curves with clear peaks of the
350 attractive forces were detected (Fig. 7B-i). In Fig. 7B-ii, the simulation snapshots show
351 that the cells exhibited highly deformed shapes or an array of regular hexagons under
352 stronger or weaker cell–cell adhesion forces (λ_{AD} = 0.9 vs. 0.0), respectively. The profiles
353 of the DF curves were quantitatively evaluated (Fig. 7B-iii); unlike the case in Fig. 3A,
354 there was a negative relationship between the cell–cell adhesion forces and the maximum
355 attractive forces (Fig. 7B-iii, left panel). In addition, the slopes of the DF curves at the
356 force = 0 —defined in Fig. 7B-iii, right panel, inset— showed negative relationship to the
357 cell–cell adhesion forces (Fig. 7B-iii, right panel). We will discuss later about these results.

358 Fig. 7C shows the inferred effective DF curves under the conditions with
359 different values of cell surface tensions. Clear distance–force curves were detected (Fig.
360 7C-i), except that abrupt changes were appeared under the stronger surface tensions (Fig.
361 7C-i, λ_S = 0.8 and 1.0). Under the stronger surface tensions, the cells showed an array of
362 regular hexagons compared with the case under the weaker surface tensions (Fig. 7C-ii).
363 The profiles of the DF curves were quantitatively evaluated (Fig. 7C-iii); unlike the case
364 in Fig. 3C, there was a positive relationship between the surface tensions and the
365 maximum attractive forces (Fig. 7C-iii, left panel). The slopes of the DF curves at the
366 force = 0 showed positive relationship to the cell surface forces (Fig. 7C-iii, right panel).
367 We interpret the meaning of the slopes of the DF curves at the force = 0 as
368 follows. In Fig. 7B-C, the maximum attractive forces show a negative or positive
369 relationship to cell–cell adhesion forces or the cell surface tensions, respectively.
370 Increased maximum attractive forces (i.e., deeper valleys in the DF curves) can lead to
371 steeper slopes of the DF curves, that is consistent with that the steeper slopes were detect
372 at the distance at the force = 0 (Fig. 7B-iii, right panel; Fig. 7C-iii, right panel). Because
373 the state of the force = 0 corresponds to a steady state, the slope at the force = 0 relates to
374 the stability of the state; i.e., in the case of a system with the steeper negative slope, when
375 the distance is slightly changed from the steady state, the force for restoring to the steady

state becomes larger. In other words, a system with the steeper slope strongly prefers to maintain cell–cell distances at a unique distance corresponding to that at the force = 0. This feature should lead to the formation of an array of regular hexagons as shown in Fig. 7B-ii and 7C-ii ($\lambda_{AD} = 0$ in B-ii or $\lambda_S = 1.0$ in C-ii). In conclusion, we think that a system preferring a regular hexagonal array shows a steeper slope accompanying a larger maximum attractive force.

In addition, we also evaluated the influence of the area elasticity (Fig. S2), and we detected no significant changes in inferred DF curves under different values of the area elasticities. We also inferred DF curves in the MDCK epithelial cells under a nearly stable state, and detected a clear DF curve with the attractive forces (Fig. S3).

DF curve in solid-liquid phase transition

As mentioned above in Fig. 7C-i, we detected an abrupt change in the profiles of the inferred DF curves. It is possible that such abrupt change corresponds to a certain phase transition. In the case of multicellular systems, solid-liquid phase transitions are well known, which are also reported in vertex models (Bi et al., 2015; Mongera et al., 2018; Petridou et al., 2021). We evaluated the fluidity of the cells in our vertex model

simulations. Fig. 8A shows the trajectories of the cell centers under the conditions of the different values of the cell surface tensions. Under the smaller values of the surface tensions (λ_S = 0.45, 0.5), the cell centers substantially moved during the simulations, indicating a liquid-like behavior. On the other hand, under the larger values of the surface tensions (λ_S = 0.8, 1.0), the positions of the cell centers were almost fixed, indicating a solid-like behavior. Fig, 8B shows the mean square displacement (MSD). MSDs were continuously increased under the weaker surface tensions (λ_S = 0.45, 0.5, 0.6), whereas MSDs reached plateaus under the stronger surface tensions (λ_S = 0.8, 1.0). Therefore, a solid-liquid transition occurs between λ_S = 0.6 and 0.8, and this critical point corresponds to the abrupt change in the inferred DF curves. We concluded that a solid-liquid phase transition was appeared as an abrupt change in the inferred DF curves.

Discussion

In the present study, we investigated how sub-cellular mechanical components relate to effective attractive/repulsive forces of cell–cell interactions in multicellular systems. By applying our particle model-based inference method to simulation outcomes generated by

412 some model frameworks such as the vertex model and the 2-particel for 1-cell model, we
413 related the effective attractive/repulsive forces to various sub-cellular mechanical
414 components. Our comprehensive analyses are summarized in Table: the cell–cell
415 adhesion forces work as effective attraction, the cell surface tensions as effective
416 repulsion, cell growth as effective repulsion, cell–ECM adhesion as effective repulsion,
417 stronger traction forces with long persistency as effective repulsion. We also added the
418 effect of egg-shells and liquid cavities as we previously reported (Koyama et al., 2024,
419 2023). Therefore, our results indicate that some sub-cellular mechanical components
420 actually work as the effective pairwise forces of cell–cell interactions. When performing
421 the cell position-based force inference method, this comprehensive description would be
422 useful to speculate the origins of the attractive/repulsive forces.

423 On the other hand, under steady states, the relationship between the effective
424 attractive/repulsive forces and the cell–cell adhesion forces/cell surface tensions was
425 changed in the vertex model (Fig. 7). Vertex models assume many-body interactions but
426 not pairwise interactions (Bi et al., 2016): the potential energies are determined through
427 the relationship among >2 cells. We guess that the effect of the many-body interactions
428 become dominant under steady states.

429 Because real tissues have many mechanical components, it is challenging to

separately measure or infer each mechanical parameter value. This is not only the case for image-based inference methods but also invasive methods including laser ablation experiments, AFM etc. For instance, by performing the laser ablation experiments, cell–cell junction tensions are estimated (Fernandez-Gonzalez et al., 2009; Ishihara and Sugimura, 2012; Koyama et al., 2016); because cell–cell junction tensions are composed of both cell–cell adhesive forces and cell surface tensions, it is difficult to dissect to what extent the two mechanical components contribute to the cell–cell junction tensions. The Young's modulus of cells can be measured by AFM, which may be affected by cell elasticities including the area elasticities, cell surface tensions, etc. Therefore, it is important to accumulate information that describes the relationships among distinct mechanical components. To this end, the theoretical analyses presented in our manuscript, together with measurements in real tissues, will serve. Although many techniques for measuring/inferring mechanical parameters have been developed, it is still challenging to do in real three-dimensional tissues. This is because of both the accessibility to the tissues and three-dimensional imaging with subsequent segmentation. We think that our cell-position based method can overcome these difficulties with parallel applications of other methods.

Conflict of Interest

The authors declare that the research was conducted in the absence of any commercial or financial relationships that could be construed as a potential conflict of interest.

Acknowledgement

We thank Ms. Azusa Kato for supporting nuclear tracking, and Drs. Kazuhiro Aoki, Yohei Kondo, and Kei Yamamoto for advices about the MDCK culture on polyacrylamide gel.

Author contribution

Conceptualization (HK, AI, HO), Data curation (HK), Formal analysis (HK), Funding acquisition (HK, TO), Investigation (HK, AI, HO, TO, KN, TF), Methodology (HK, KN), Project administration (HK), Resources (HK, TO, TF), Supervision (TF), Validation (HK), Visualization (HK), Writing – original draft (HK), Writing – review and editing (HK, AI, HO, TO, KN, TF)

Funding

This work was supported by following grants: the National Institutes of Natural Sciences (NINS) program for cross-disciplinary science study for H.K., a Japan Society for the

Promotion of Science (JSPS) Grant-in-Aid for Young Scientists (B) for H.K. (17K15131), for Scientific Research (C) for T.O. (18K06234), and for Young Scientists (B) for T.O. (16K18544), and for Transformative Research Areas (A) for HK (24H01990, 24H01414), a MEXT/JSPS Grant-in-Aid for Scientific Research on Innovative Areas for T.O. (17H05627), the Inamori Foundation for T.O., and the Takeda Science Foundation for T.O.

Declaration of generative AI and AI-assisted technologies

During the preparation of this work the authors used DeepL in order to improve the readability of the manuscript. After using this tool, the authors reviewed and edited the content as needed and take full responsibility for the content of the published article.

References

Aoki, K., Kondo, Y., Honda, N., Hiratsuka, T., Itoh, R.E., Matsuda, M., 2017. Propagating Wave of ERK Activation Orients Collective Cell Migration. Dev. Cell 43, 305–317. https://doi.org/10.1016/j.devcel.2017.10.016

Atkins, P., Paula, J. De, Keeler, J., 2018. Atkins' Physical Chemistry, 11th ed. ed.

Oxford University Press.

Basan, M., Prost, J., Joanny, J.-F., Elgeti, J., 2011. Dissipative particle dynamics simulations for biological tissues: rheology and competition. Phys. Biol. 8, 026014.

Bi, D., Lopez, J.H., Schwarz, J.M., Manning, M.L., 2015. A density-independent rigidity transition in biological tissues. Nat. Phys. 11, 1074–1079. https://doi.org/10.1038/NPHYS3471

Bi, D., Yang, X., Marchetti, M.C., Manning, M.L., 2016. Motility-driven glass and jamming transitions in biological tissues. Phys. Rev. X 6, 021011. https://doi.org/10.1103/PhysRevX.6.021011

Brodland, G.W., Conte, V., Cranston, P.G., Veldhuis, J., Narasimhan, S., Hutson, M.S., Jacinto, A., Ulrich, F., Baum, B., Miodownik, M., 2010. Video force microscopy reveals the mechanics of ventral furrow invagination in Drosophila. Proc. Natl. Acad. Sci. U. S. A. 107, 22111–22116. https://doi.org/10.1073/pnas.1006591107

Campàs, O., 2016. A toolbox to explore the mechanics of living embryonic tissues. Semin. Cell Dev. Biol. 55, 119–130. https://doi.org/10.1016/j.semcdb.2016.03.011

Delile, J., Herrmann, M., Peyriéras, N., Doursat, R., 2017. A cell-based computational model of early embryogenesis coupling mechanical behaviour and gene regulation. Nat. Commun. 8, 13929. https://doi.org/10.1038/ncomms13929

Drasdo, D., Kree, R., McCaskill, J.S., 1995. Monte Carlo approach to tissue-cell populations. Phys. Rev. E 52, 6635–6657.

Fernandez-Gonzalez, R., Simoes, S.D.M., Röper, J.C., Eaton, S., Zallen, J.A., 2009. Myosin II Dynamics Are Regulated by Tension in Intercalating Cells. Dev. Cell 17, 736–743. https://doi.org/10.1016/j.devcel.2009.09.003

Fletcher, A.G., Osterfield, M., Baker, R.E., Shvartsman, S.Y., 2014. Vertex models of epithelial morphogenesis. Biophys. J. 106, 2291–2304. https://doi.org/10.1016/j.bpj.2013.11.4498

Forgacs, G., Newman, S.A., 2005. Biological Physics of the Developing Embryo. Cambridge University Press.

Garcia, S., Hannezo, E., Elgeti, J., Joanny, J.F., Silberzan, P., Gov, N.S., 2015. Physics of active jamming during collective cellular motion in a monolayer. Proc. Natl. Acad. Sci. U. S. A. 112, 15314–15319. https://doi.org/10.1073/pnas.1510973112

Guillot, C., Lecuit, T., 2013. Mechanics of epithelial tissue homeostasis and morphogenesis. Science (80-.). 340, 1185–9. https://doi.org/10.1126/science.1235249

He, B., Doubrovinski, K., Polyakov, O., Wieschaus, E., 2014. Apical constriction drives tissue-scale hydrodynamic flow to mediate cell elongation. Nature 508, 392–396.

https://doi.org/10.1038/nature13070

Honda, H., Motosugi, N., Nagai, T., Tanemura, M., Hiiragi, T., 2008. Computer simulation of emerging asymmetry in the mouse blastocyst. Development 135, 1407–1414. https://doi.org/10.1242/dev.014555

Ishihara, S., Sugimura, K., 2012. Bayesian inference of force dynamics during morphogenesis. J. Theor. Biol. 313, 201–211. https://doi.org/10.1016/j.jtbi.2012.08.017

Israelachvili, J.N., 2011. Intermolecular and Surface Forces, 3rd ed. ed. Elsevier Inc.

Kajita, A., Yamamura, M., Kohara, Y., 2003. Computer simulation of the cellular arrangement using physical model in early cleavage of the nematode Caenorhabditis elegans. Bioinformatics 19, 704–716. https://doi.org/10.1093/bioinformatics/btg069

Koyama, H., Okumura, H., Ito, A.M., Nakamura, K., Otani, T., Kato, K., Fujimori, T., 2023. Effective mechanical potential of cell–cell interaction explains three-dimensional morphologies during early embryogenesis. PLoS Comput. Biol. 19, e1011306. https://doi.org/10.1371/journal.pcbi.1011306

Koyama, H., Okumura, H., Otani, T., Ito, A.M., Nakamura, K., Kato, K., Fujimori, T., 2024. Effective mechanical potential of cell–cell interaction in tissues harboring

cavity and in cell sheet toward morphogenesis. Front. Cell Develpmental Biol. 12, doi: 10.3389/fcell.2024.1414601. https://doi.org/10.3389/fcell.2024.1414601

Koyama, H., Shi, D., Suzuki, M., Ueno, N., Uemura, T., Fujimori, T., 2016. Mechanical Regulation of Three-Dimensional Epithelial Fold Pattern Formation in the Mouse Oviduct. Biophys. J. 111, 650–665. https://doi.org/10.1016/j.bpj.2016.06.032

Koyama, H., Suzuki, M., Yasue, N., Sasaki, H., Ueno, N., 2022. Differential Cellular Stiffness Contributes to Tissue Elongation on an Expanding Surface. Front. Cell Develpmental Biol. 10, 864135. https://doi.org/10.3389/fcell.2022.864135

Landsberg, K.P., Farhadifar, R., Ranft, J., Umetsu, D., Widmann, T.J., Bittig, T., Said, A., Jülicher, F., Dahmann, C., 2009. Increased Cell Bond Tension Governs Cell Sorting at the Drosophila Anteroposterior Compartment Boundary. Curr. Biol. 19, 1950–1955. https://doi.org/10.1016/j.cub.2009.10.021

Lecuit, T., Lenne, P.-F., Munro, E., 2011. Force Generation, Transmission, and Integration during Cell and Tissue Morphogenesis. Annu. Rev. Cell Dev. Biol. 27, 157–184. https://doi.org/10.1146/annurev-cellbio-100109-104027

Li, X., Balagam, R., He, T.-F., Lee, P.P., Igoshin, O.A., Levine, H., 2017. On the mechanism of long-range orientational order of fibroblasts. Proc. Natl. Acad. Sci. 114, 8974–8979. https://doi.org/10.1073/pnas.1707210114

Maître, J.-L., Berthoumieux, H., Krens, S.F.G., Salbreux, G., Jülicher, F., Paluch, E., Heisenberg, C.P., 2012. Adhesion Functions in Cell Sorting by Mechanically Coupling the Cortices of Adhering Cells. Science (80-.). 338, 253–256. https://doi.org/10.1126/science.1225399

Marinari, E., Mehonic, A., Curran, S., Gale, J., Duke, T., Baum, B., 2012. Live-cell delamination counterbalances epithelial growth to limit tissue overcrowding. Nature 484, 542–545. https://doi.org/10.1038/nature10984

Merkel, M., Manning, M.L., 2017. Using cell deformation and motion to predict forces and collective behavior in morphogenesis. Semin. Cell Dev. Biol. 67, 161–169. https://doi.org/10.1016/j.semcdb.2016.07.029

Mongera, A., Rowghanian, P., Gustafson, H.J., Shelton, E., Kealhofer, D.A., Carn, E.K., Serwane, F., Lucio, A.A., Giammona, J., Campàs, O., 2018. A fluid-to-solid jamming transition underlies vertebrate body axis elongation. Nature 561, 401–405. https://doi.org/10.1038/s41586-018-0479-2

Nissen, S.B., Perera, M., Gonzalez, J.M., Morgani, S.M., Jensen, M.H., Sneppen, K., Brickman, J.M., Trusina, A., 2017. Four simple rules that are sufficient to generate the mammalian blastocyst. PLoS Biol. 15, e2000737. https://doi.org/10.1371/journal.pbio.2000737

Nissen, S.B., Rønhild, S., Trusina, A., Sneppen, K., 2018. Theoretical tool bridging cell polarities with development of robust morphologies. Elife 7, e38407. https://doi.org/10.7554/elife.38407

Nonomura, M., 2012. Study on multicellular systems using a phase field model. PLoS One 7, 1–9. https://doi.org/10.1371/journal.pone.0033501

Okuda, S., Inoue, Y., Adachi, T., 2015. Three-dimensional vertex model for simulating multicellular morphogenesis. Biophys. Physicobiology 12, 13–20. https://doi.org/10.2142/biophysico.12.0

Pérez-González, C., Alert, R., Blanch-Mercader, C., Gómez-González, M., Kolodziej, T., Bazellieres, E., Casademunt, J., Trepat, X., 2019. Active wetting of epithelial tissues. Nat. Phys. 15, 79–88. https://doi.org/10.1038/s41567-018-0279-5

Petridou, N.I., Corominas-Murtra, B., Heisenberg, C.P., Hannezo, E., 2021. Rigidity percolation uncovers a structural basis for embryonic tissue phase transitions. Cell 184, 1914-1928.e19. https://doi.org/10.1016/j.cell.2021.02.017

Podewitz, N., Delarue, M., Elgeti, J., 2015. Tissue homeostasis: A tensile state. Epl 109, 1–6. https://doi.org/10.1209/0295-5075/109/58005

Ranft, J., Basan, M., Elgeti, J., Joanny, J.-F., Prost, J., Jülicher, F., 2010. Fluidization of tissues by cell division and apoptosis. Proc. Natl. Acad. Sci. U. S. A. 107, 20863–

20868. https://doi.org/10.1073/pnas.1011086107

Ryan, P.L., Foty, R.A., Kohn, J., Steinberg, M.S., 2001. Tissue spreading on implantable substrates is a competitive outcome of cell–cell vs . cell–substratum adhesivity. Proc. Natl. Acad. Sci. U. S. A. 98, 4323–4327.

Schötz, E., Burdine, R.D., Jülicher, F., Steinberg, M.S., Heisenberg, C.P., Foty, R.A., 2008. Quantitative differences in tissue surface tension influence zebrafish germ layer positioning. HFSP J. 2, 42–56. https://doi.org/10.2976/1.2834817

Steinberg, M.S., 2007. Differential adhesion in morphogenesis : a modern view. Curr. Opin. Genet. Dev. 17, 1281–286. https://doi.org/10.1016/j.gde.2007.05.002

Sugimura, K., Lenne, P., Graner, F., 2016. Measuring forces and stresses in situ in living tissues 186–196. https://doi.org/10.1242/dev.119776

Suzuki, M., Sato, M., Koyama, H., Hara, Y., Hayashi, K., Yasue, N., Imamura, H., Fujimori, T., Nagai, T., Campbell, R.E., Ueno, N., 2017. Distinct intracellular Ca 2 + dynamics regulate apical constriction and differentially contribute to neural tube closure. Development 144, 1307–1316. https://doi.org/10.1242/dev.141952

Szabó, B., Szöllösi, G.J., Gönci, B., Jurányi, Z., Selmeczi, D., Vicsek, T., 2006. Phase transition in the collective migration of tissue cells: Experiment and model. Phys. Rev. E 74, 061908. https://doi.org/10.1103/PhysRevE.74.061908

Yong, J., Moeller, J., Hart, K.C., Ramallo, D., Vogel, V., Dunn, A.R., Nelson, W.J., Pruitt, B.L., 2015. Spatial distribution of cell–cell and cell–ECM adhesions regulates force balance while maintaining E-cadherin molecular tension in cell pairs. Mol. Biol. Cell 26, 2456–2465. https://doi.org/10.1091/mbc.E14-12-1618

Zimmermann, J., Camley, B.A., Rappel, W., Levine, H., 2016. Contact inhibition of locomotion determines cell – cell and cell – substrate forces in tissues. Proc. Natl. Acad. Sci. https://doi.org/10.1073/pnas.1522330113

Figures

Figure 1: Attractive/repulsive forces of cell–cell interactions

A. Microscopic forces contributing to cell–cell interactions are exemplified in the case of isolated two cell system.

B. The microscopic forces are approximated as attractive/repulsive forces in particle models.

C. Both the repulsive and attractive forces are provided as cell–cell distance-dependent functions, and the summation (black broken line) is the distance–force curve of the two particles. The relationship between the curve and the mean diameters of the cells is shown.

D. Sub-cellular mechanical components in multicellular systems include cell–cell adhesion forces, cell surface tensions, etc. They can be the origin of the effective attractive/repulsive forces.

Figure 2: Inference of effective attractive/repulsive of cell–cell interaction in vertex model

A. Vertex model. λ_{Tot} is the line tension exerted on cell–cell junctions or on cellular edges of outer boundary. The potential energy on a junction or edge is $\lambda_{\mathrm{Tot}} L^{<k,l>}$, where L is the

length of the junction or edge composed of *k*th and *l*th vertices. The potential energy for a cell provided by the area elasticity is $(1/2)K_{\mathrm{a}}\left(a_n / a_{\mathrm{o}} - 1\right)^2 a_{\mathrm{o}}$, where a_n is the area of *n*th cell and a_{o} is the natural area. An example of simulations is shown with the parameter values in the right panel. In addition to the cell contours, cell centers are shown as dots.

B. Inferred effective distance–force (DF) curves under various values of the fluctuations of tension, σ. i) The inferred forces are plotted against cell–cell distances, and averaged values of the forces are shown in yellow (binned average). ii) Inferred DF curves which were obtained by calculating the binned average.

Figure 3: Effective attractive/repulsive forces in vertex model

A. Inferred DF curves under various values of cell–cell adhesive forces, λ_{AD}. i) Simulation outcomes are shown where the cell cluster tends to form a circular colony under increased values of the adhesive forces ($\lambda_{\mathrm{AD}} = 0.9$). Cell centers are shown as dots. ii) Inferred DF curves. iii) Quantitative comparison of the DF curves.

B. Inferred DF curves under various values of cell surface tensions, λ_{S}. i) Inferred DF curves. ii) Quantitative comparison of the DF curves.

C. Inferred DF curves under various values of area elasticities, K_{a}. i) Inferred DF curves.

ii) Quantitative comparison of the DF curves.

Figure 4: Effective attractive/repulsive forces in the presence of cell-ECM adhesion

Cell–ECM adhesion energy is assumed in the vertex model used in Fig. 3. i) The energy for a cell is defined as $-E_{\mathrm{ECM}}a_n$, where E_{ECM} is the coefficient of the energy. ii) Simulation outcomes are exemplified where the cell areas are increased under larger value of E_{ECM}. The left and right panels are shown with the same scale. iii) Inferred DF curves. iv) Quantitative comparisons of the DF curves.

Figure 5: Effective attractive/repulsive forces in the presence of cell-ECM traction forces

A. Traction forces between cells and ECM are assumed in the particle model under two-dimensional conditions. i) Cell–cell interaction forces are provided by the LJ potential. The directions of the traction forces are random. ii) An example of simulations is shown. iii and iv) Inferred DF curves under various values of the traction forces and under various values of the persistency, respectively. The distance–force curve provided by the LJ potential is also shown (broken black lines).

B. Traction forces are assumed to have the same vector (i.e., the same value and the same direction). i) An example of simulations is shown. Due to the same vector, the particles migrated unidirectionally. ii) Inferred DF curves under various values of the traction forces. The distance–force curve provided by the LJ potential is also shown.

Related Figures: Figure S1 (inference in self-migratory MDCK cells on substrates)

Figure 6: Effective attractive/repulsive forces in growing cells

i) Model of cell growth. Orange, a cell; green, particle. The growth force between the two particles is provided as defined in the main text, where C = 5.6 and D_{CR} = 5.0. The distance–force curve provided by the LJ potential was set to have the maximum attractive force = 0.005. Therefore, when B = 0.5 and D = 4.4, the repulsive force given from the growth becomes 0.005, equivalent to the attractive force of the LJ. ii) Examples of simulations under different values of B, where the particles but not the cells are visualized. iii) Inferred DF curves. iv) Quantitative comparison of the DF curves.

Figure 7: Effective attractive/repulsive forces under steady state

A. Examples of vertex model simulations under steady state. The vertex model models used are the same as that in Fig. 2. Cell centers are shown as crosses. The whole view of the simulation is shown in Fig. S2.

B. Inferred DF curves under various values of the cell–cell adhesive forces, λ_{AD}. i) Inferred DF curves. ii) Simulation outcomes. iii) Quantitative comparisons of the DF curves.

C. Inferred DF curves under various values of the cell surface tensions, λ_S. i) Inferred DF curves. ii) Simulation outcomes. iii) Quantitative comparisons of the DF curves.

Related Figures: Figure S2 (whole view of the simulations, and inferred DF curves under various values of the area elasticities, K_a), Figure S3 (inferred DF curves in the MDCK cells under steady states)

Figure 8: Solid-liquid phase transition in vertex model

A. Trajectories of cell centers in the vertex model in Fig. 7 are shown under various values of the cell surface tensions. The sizes of each window correspond to those in the simulation snapshots of Fig. 7.

B. The mean square displacements (MSD) are shown under various values of the cell

surface tensions.

Table 1: Effect of cellular and non-cellular factors on effective force of cell−cell interaction

	Influence to force (attractive or repulsive)		Figures
Cellular factors			
cell−cell adhesion	attractive		3A
cell surface tension	repulsive		3B
area elasticity	neutral	core stiffness increased?	3C
cell growth	repulsive		6
Non-cellular factors			
cell-ECM adhesion	repulsive		4
cell-ECM traction force			
i. random direction	neutral/repulsive		5A
ii. uniform	neutral		5B
egg-shell	neutral		Ref. 1
cavity			
i. expanding	repulsive		Ref. 2
ii. non-expanding	neutral		Ref. 2

Ref. 1; (Koyama et al., 2023). Ref .2 ; (Koyama et al., 2024)

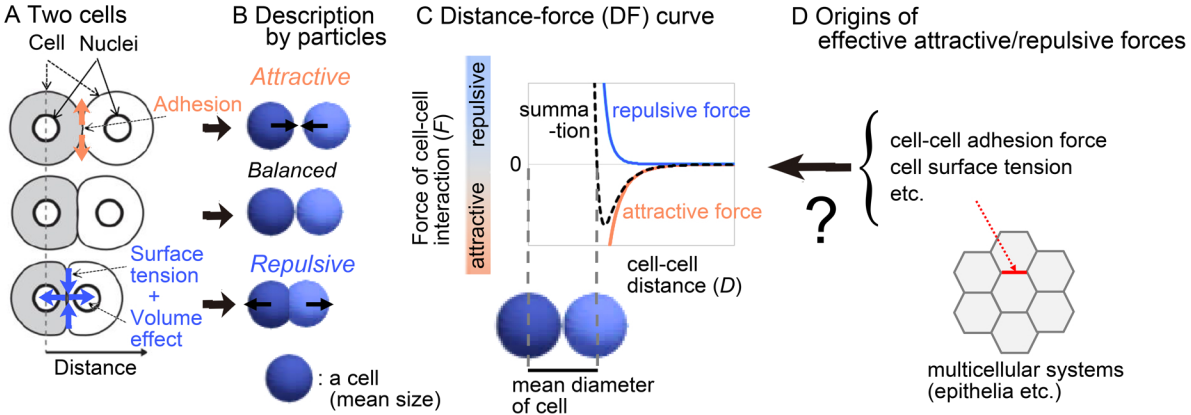

Fig.1 Koyama et al.

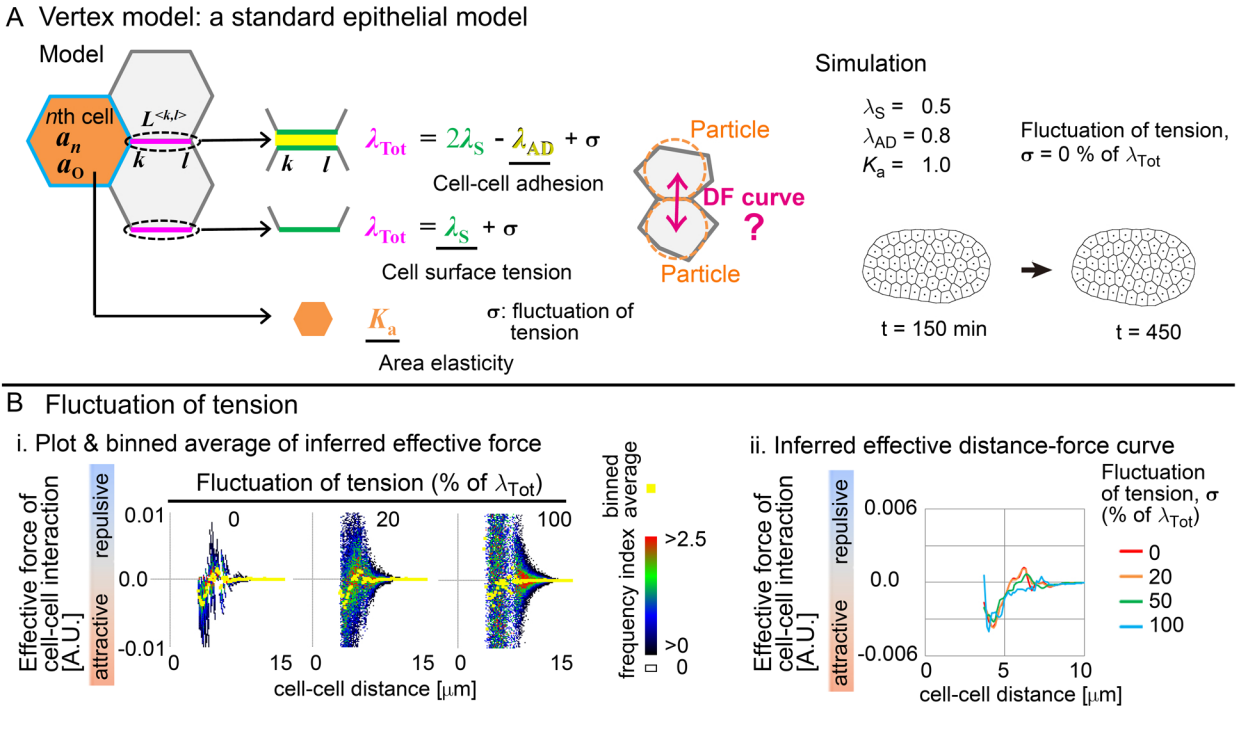

Fig.2 Koyama et al.

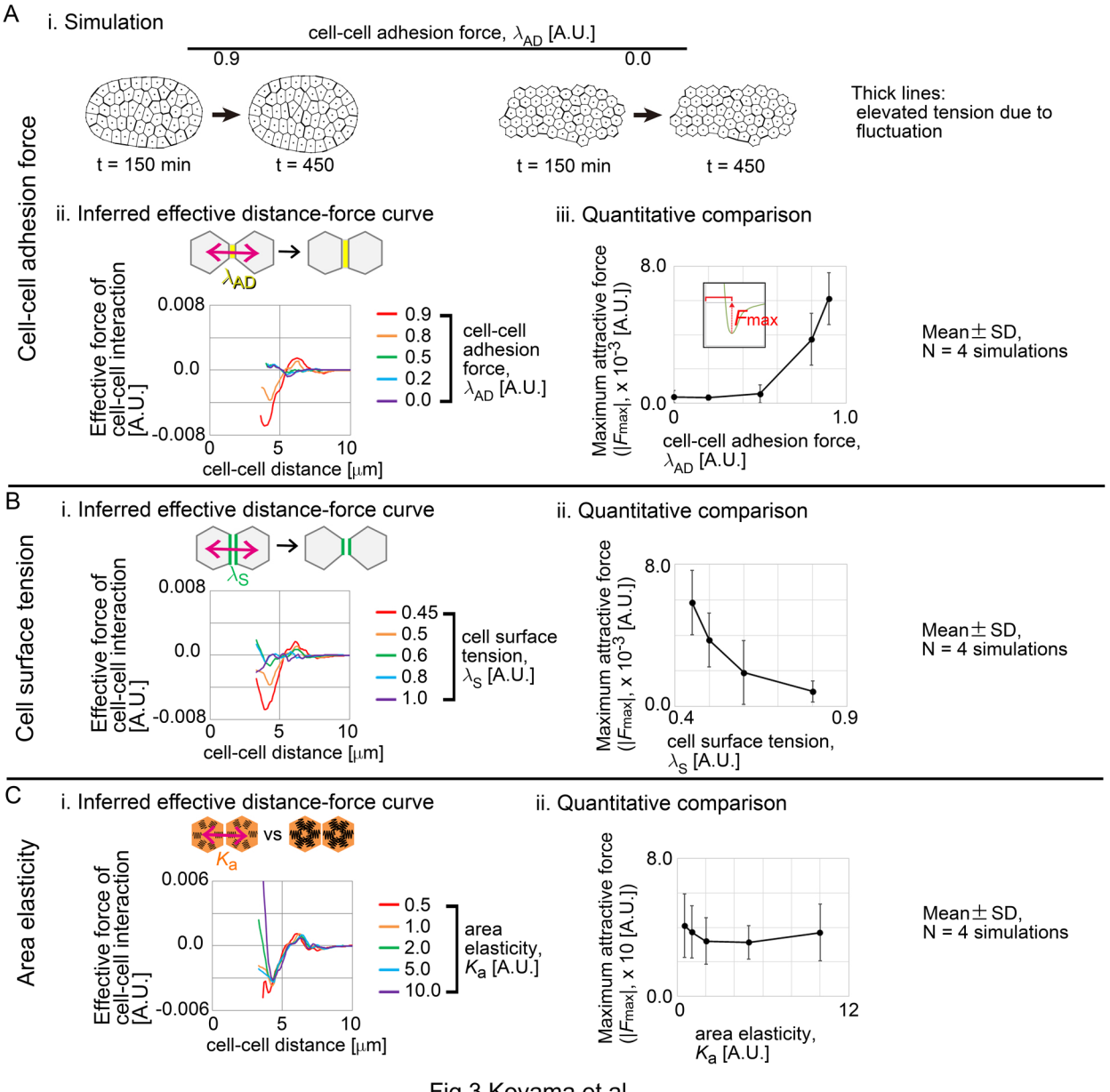

Fig.3 Koyama et al.

Cell-ECM adhesion energy

i. Vertex model with cell-ECM adhesion

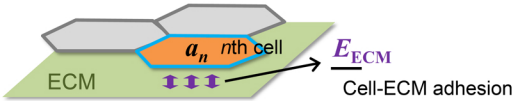

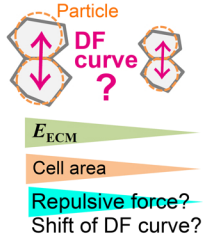

ii. Simulation

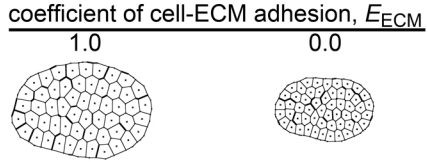

iii. Inferred effective distance-force curve

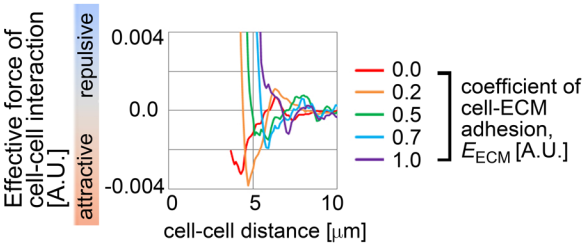

iv. Quantitative comparisons

Mean ± SD,
N = 4 simulations

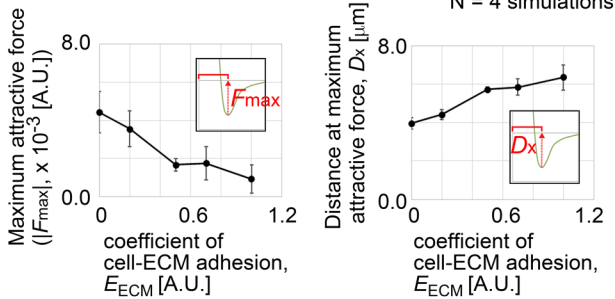

Fig.4 Koyama et al.

A Traction force of random direction between cell-ECM

i. Particle model with traction force

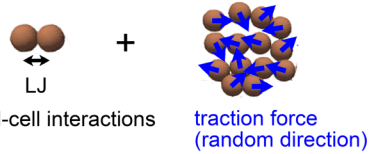

ii. Simulation (2-dimension)

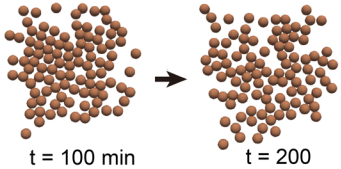

maximum attractive force of LJ = 0.01

traction force = 0.1 (1,000% of LJ) with persistency = 50.0 min

iii. Inferred effective distance-force curve
effect of traction force value

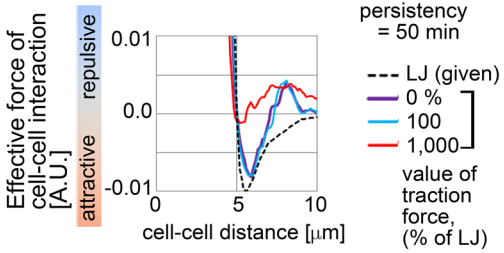

iv. Inferred effective distance-force curve
effect of persistency of traction force

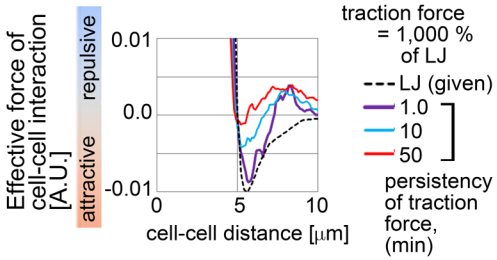

B Systems with traction force of uniform vector

i. Model & simulation

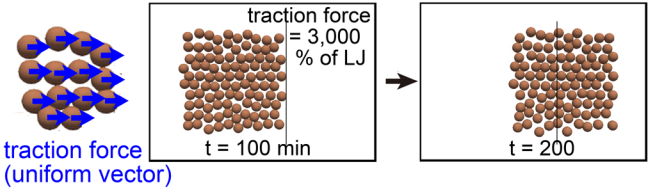

ii. Inferred effective distance-force curve

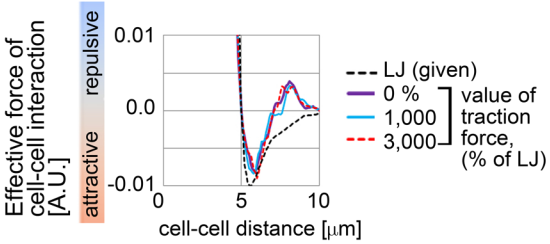

Fig.5 Koyama et al.

Cell growth

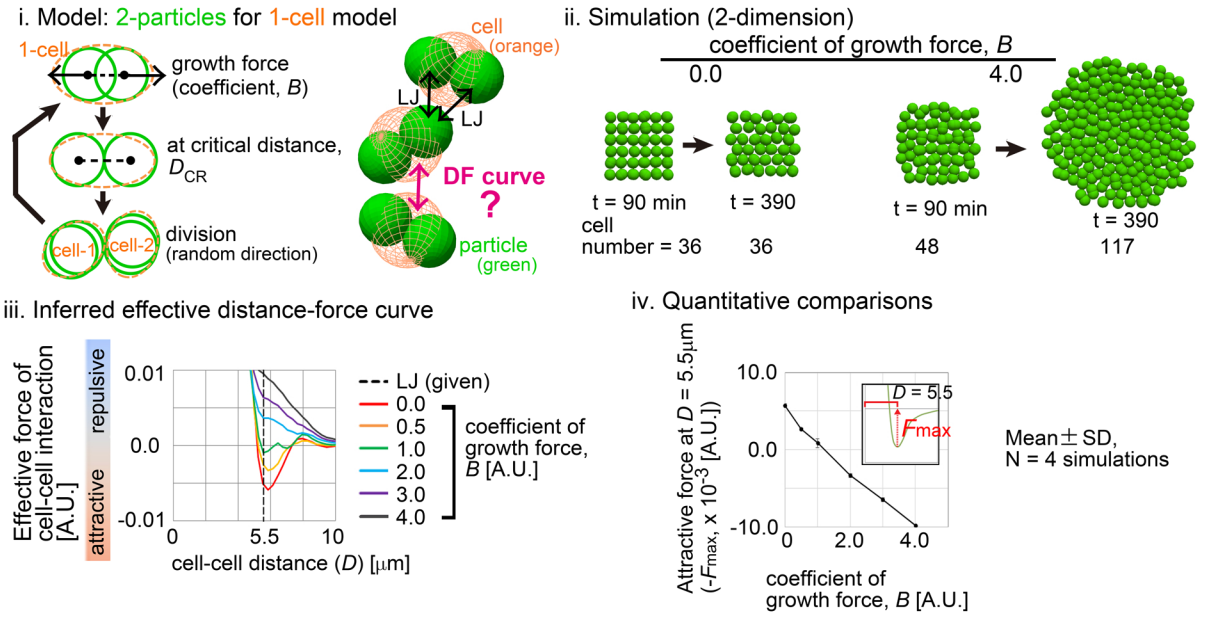

Fig.6 Koyama et al.

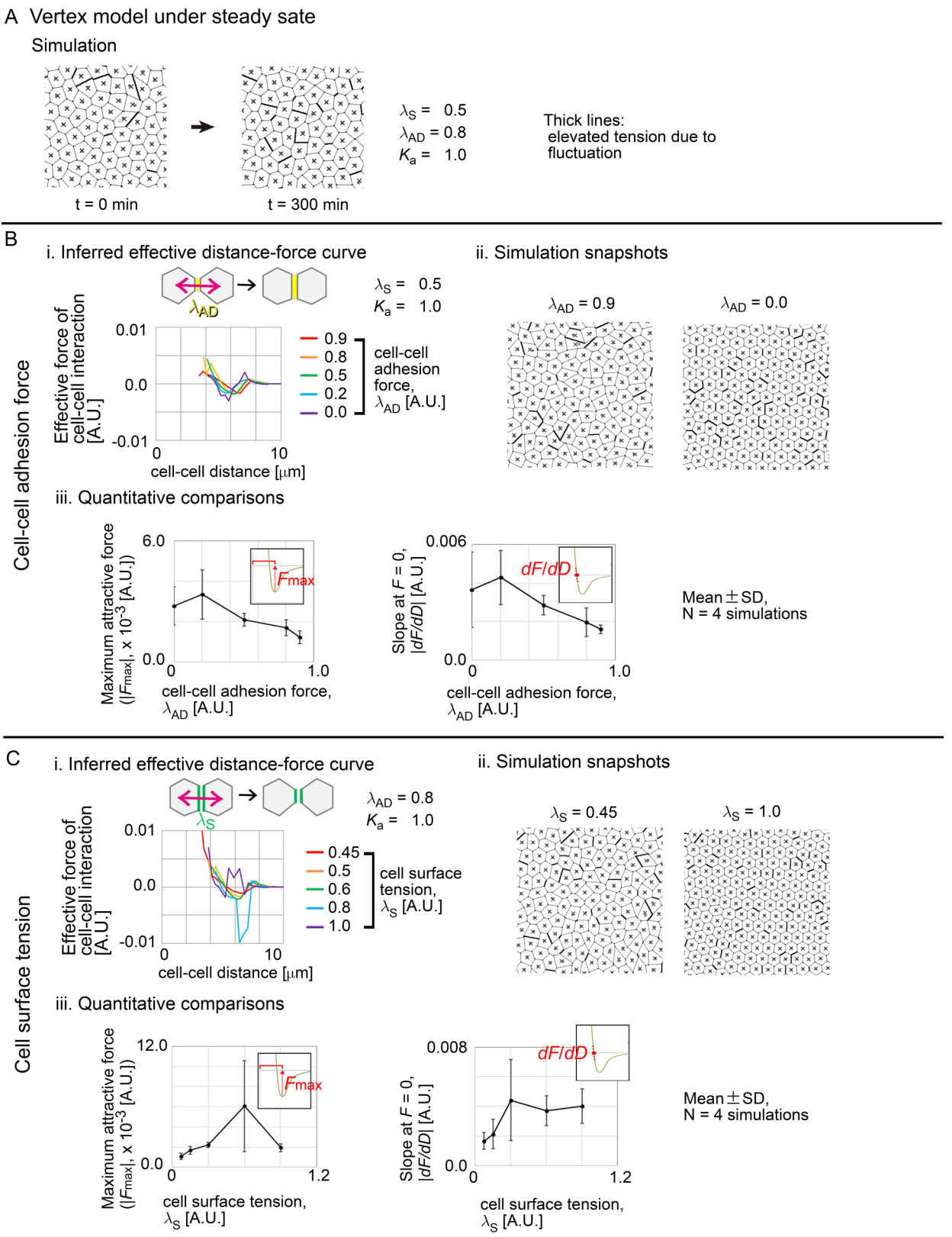

Fig.7 Koyama et al.

A Trajectory of cell center in vertex model

Simulation

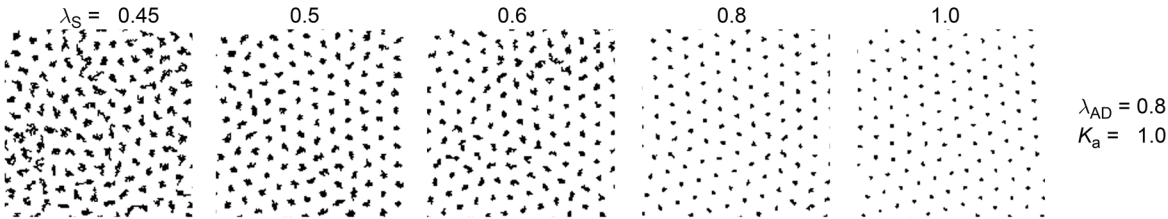

B Mean square displacement

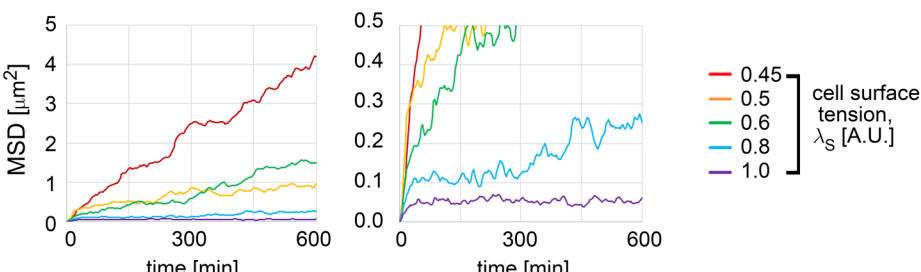

Fig.8 Koyama et al.